Bai, Y., He, Y., Yuan, X., Tilmann, F., Ai, Y., Jiang, M., Hou, G., Mon, C. T., Thant, M., Sein, K. (2021): Seismic structure across central Myanmar from joint inversion of receiver functions and Rayleigh wave dispersion. - Tectonophysics, 818, 229068.

https://doi.org/10.1016/j.tecto.2021.229068

Seismic Structure Across Central Myanmar from Joint Inversion of Receiver Functions and Rayleigh Wave Dispersion

Yiming Bai[a,b,d], Yumei He[a,c,d], Xiaohui Yuan[b], Frederik Tilmann[b,e], Yinshuang Ai[a,c,d,*], Mingming Jiang[a,c,d], Guangbing Hou[a], Chit Thet Mon[a,f], Myo Thant[g], Kyaing Sein[h]

[a]Key Laboratory of Earth and Planetary Physics, Institute of Geology and Geophysics, Chinese Academy of Sciences, 100029, Beijing, China.

[b]Deutsches GeoForschungsZentrum GFZ, 14473, Potsdam, Germany.

[c]Innovation Academy for Earth Science, Chinese Academy of Sciences, 100029, Beijing, China.

[d]College of Earth and Planetary Sciences, University of Chinese Academy of Sciences, 100049, Beijing, China.

[e]Freie University of Berlin, Malteserstr. 74-100, 12249, Berlin, Germany.

[f]Department of Geology, Dagon University, Yangon, Myanmar.

[g]Department of Geology, University of Yangon, 11041, Yangon, Myanmar.

[h]Myanmar Geosciences Society, Yangon, Myanmar.

[*]Corresponding author: Yinshuang Ai (ysai@mail.iggcas.ac.cn)

Abstract

The active tectonics in Myanmar is governed by the ongoing northward indentation and obliquely-eastward subduction of India into Eurasia. So far, detailed seismic structure of the crust and uppermost mantle at the eastern flank of the India-Eurasia collision zone remains highly debated. With seismic waveforms recorded at 79 broadband stations in Myanmar, we build a regional shear velocity model in the depth range of 0-80 km by joint inversion of ambient noise derived Rayleigh wave dispersion and P-wave receiver functions. Common conversion point stacking was performed along two representative profiles. We observe clear variations in the seismic velocity and discontinuity structures beneath this region. 1) A sedimentary layer covers the eastern fore-arc trough of the Central Myanmar Basin, with shear velocity less than 2.5 km/s and thickness increasing from ~8 km at 22°N to ~18 km at 23°N. The fore-arc Chindwin basin is evidently thicker than the back-arc Shwebo basin, an abrupt eastward drop in sediment thickness appears immediately below the Wuntho-Popa magmatic arc. 2) Crustal low-velocity (LV) anomalies (< 3.3 km/s) in the Indo-Burma Ranges probably reflect the Bengal sediments accreted to the toe of the overlying Burma plate, 3) The underlying LV layer with a thickness of over 25 km below the Burma Moho (30-40 km in depth) is indicative of the eastward subduction of the Indian continental crust, the top boundary of which is imaged with a dip angle of ~20°. 4) Upper mantle LV anomalies filling the majority of the back-arc domain at depths greater than 60 km display a connection to a small-scale, subcrustal LV body beneath the Monywa volcano, possibly forming a fluid- or melt-rich mantle channel.

Keywords: Myanmar, Subduction zone, Joint inversion, S-wave velocity structure, Seismic discontinuity

1. Introduction

The northward collision of the Indian plate into the Eurasian plate since the Eocene has resulted in the rise of the Himalayan orogen and the Tibetan plateau (e.g., Molnar and Stock, 2009). Recent seismological studies have demonstrated the sub-horizontal subduction of the Indian plate beneath the Tibetan plateau (e.g., Li et al., 2008; Zhao et al., 2010). Trigged by the Indian indentation, eastward escape of the upper crustal material out of the plateau has been indicated by the GPS velocity field showing clockwise rotation around the Eastern Himalayan syntaxis (e.g., Zhang et al., 2004). The collisional front along the Himalayans is ended to the east by the eastern syntaxis and pivots southwards into western Myanmar. There, the mode of convergence shifts dramatically from underthrusting to hyper-oblique subduction, which is responsible for the formation of the Burma micro-plate, a fore-arc sliver anchored to the Indian plate (e.g., Satyabala, 2003; Rangin et al., 2013). In order to unravel the complex tectonic evolution at the eastern margin of the Indian plate and its associated seismicity and volcanism, it is key to investigating detailed seismic velocity structure beneath Myanmar.

Our study region lies mostly in central Myanmar and composes of several N-S oriented tectonic elements (Figure 1). The Indo-Burma Ranges (IBR) in the west are an arcuate fold-and-thrust belt mainly formed by Eocene flysch sediments, early Cretaceous ophiolites and a high-grade metamorphic core (Mitchell, 1993; Maurin and Rangin, 2009; Morley et al., 2020). East of the IBR adjacent to the Kabaw fault, the Central Myanmar Basin (CMB) is filled with late Cretaceous-Quaternary sediments up to 18 km thick (Pivnik et al., 1998). The mid-Cretaceous Wuntho-Popa magmatic arc, with sporadically distributed volcanics on the surface, further splits the thick fore-arc basin in the west from the thinner back-arc basin in the east (Bender, 1983; Mitchell, 1993; Bertrand and Rangin, 2003; Licht et al., 2018). The active strike-slip Sagaing fault cuts across the CMB in the eastern flank and links the Andaman spreading system in the south. Farther east, the Shan Plateau (SP) belongs to the Sibumasu Block and consists primarily of Cambrian to early Cretaceous sequences, with the Mogok metamorphic belt fringing its west (Mitchell, 1993; Metcalfe, 2011).

Influenced by the obliquely-eastward subduction of the Indian plate, this area is of high seismic risk. East of the magmatic arc, seismic activities mostly concentrate around active fault zones within the Burma crust (Mon et al., 2020). One of the greatest seismic hazards in Myanmar results from shallow strike-slip earthquakes along the Sagaing fault, posing a grave danger to its nearby population centers (Hurukawa and Maung Maung, 2011). In the middle study region, near-surface sedimentary rocks in the CMB can cause significant amplification and resonances to the long period ground motions triggered by earthquakes (e.g., Borcherdt and Gibbs, 1976). Farther west, beneath the IBR, seismicity changes from predominately dextral strike-slip mechanism to mixed thrust and strike-slip (Kumar et al., 2015). An east-dipping Benioff zone with hypocenters down to ~180 km depth highlights the existence of the subducted Indian plate (Ni et al., 1989; Hurukawa et al., 2012). In order to accurately locate earthquakes and to help assess the diverse seismogenesis in this area, it is important to acquire detailed geometry of the subsurface structure.

Existing tomographic images show that the Indian slab of high seismic velocity material has descended far beyond local seismicity into the upper mantle beneath Myanmar (e.g., Li et al., 2008; Pesicek et al., 2010; Koulakov, 2011; Yao et al., 2021). However, the majority of these studies concentrate on the upper mantle velocity features beneath Myanmar, and thus provide limited information on the shallow (i.e., <100 km depth) structure of the study region. Since digital broadband networks began to be set up in 2016, regional 3-D crustal shear velocity model of Myanmar have been obtained by either joint inversion of receiver functions (RFs), Rayleigh wave dispersion and ellipticity (Wang et al., 2019) or ambient noise tomography (Wu et al., 2021). These models provide constraints on the main structures such as the sedimentary basin and the Moho discontinuity, but the average station spacing in these studies was ~150 km. Using data retrieved from a denser seismic network, both RFs (Zheng et al., 2020) and local earthquake tomography (Zhang et al., 2021) reveal an east-trending low velocity layer down to a depth of ~100 km, suggesting the subduction of the Indian continental crust below central Myanmar.

Benefiting from a recently-deployed dense 2-D seismic network and other available permanent stations in central Myanmar, we refine the regional shear velocity structure by joint inversion of ambient noise derived Rayleigh wave dispersion and RFs. By combining information from surface wave dispersion and RFs, the inverted shear velocity model well constrains both vertical and lateral velocity variations. To better interpret the joint inversion pictures, we also performed common conversion point (CCP) stacking of the RFs along two representative profiles. Integrated with existing observations, we then relate the dominant features presented in our new shear velocity model and CCP stacked profiles to the tectonic processes along the eastern margin of the Indian plate.

2. Data processing

We analyzed the ambient noise and teleseismic body wave data recorded between June 2016 and January 2018 by 70 temporary broadband stations from the CMGSMO network (Bai et al., 2020; Mon et al., 2020; Zhang et al., 2021) and 9 permanent stations, 8 of which are from the Myanmar National Seismic Network and 1 from the GE network (Figure 1). The average spacing between stations is less than 50 km, which provides an unprecedented opportunity to study detailed crustal and uppermost mantle structure beneath central Myanmar.

2.1 Ambient noise correlation and tomography

Surface wave dispersion inferred by ambient noise interferometry is not reliant on a good azimuthal distribution of earthquakes and has become a powerful tool for imaging subsurface velocity structure at local scale (e.g., Shapiro and Campillo, 2004; Shapiro et al., 2005). We processed ambient noise data following the procedures described by Bensen et al. (2007). For each station, vertical components of continuous seismic waveforms were cut into day-length segments. After removal of mean, trend, and instrument response, the data were down-sampled to 1 Hz and bandpass filtered at 2-100 s. Temporal running-absolute-mean normalization and spectral whitening were carried out to suppress the effects of earthquake signals and instrumental irregularities. Subsequently, daily inter-station cross correlations were computed and then linearly stacked for each station pair. Figure S1 shows an example of cross correlations between station M20 and the other stations used. Apparently, Rayleigh wave signals are more complicated and propagate much slower on inter-station paths across the western study region than those in the east. To further improve the signal-to-noise ratio, we averaged the positive and negative correlation lags for dispersion analysis.

The inter-station group and phase velocity dispersion curves of the fundamental-mode Rayleigh wave were extracted by an image transformation technique (Yao et al., 2006). We selected reliable dispersion measurements based on two criteria: (1) the inter-station distance should be at least 1.5 times the wavelength and (2) the signal-to-noise ratio of cross correlations, defined as the peak amplitude in the signal window divided by the mean amplitude in the noise window, are more than 5. In addition, we ensured the smoothness and coherence of the dispersion curves through manual inspection. In some cases where dispersion curves exhibit abrupt disconnections, the velocity measurements at shorter periods (e.g., less than 10-15 s) would be discarded. Figure S2 shows an example of dispersion curves extracted between two stations located in the CMB. Eventually, we acquired group and phase velocity dispersion curves at the period band of 3-40 s, with more than 1000 measurements made available at most periods. (Figure S3).

We adopted the Fast Marching Surface Tomography (FMST) approach (Rawlinson and Sambridge, 2005) to invert for the 2-D Rayleigh wave velocity maps at individual period from 3 to 40 s. We meshed our study region into a grid with 0.2° spacing in both longitude and latitude. As starting model each grid node was specified to the velocity averaged on all inter-station paths at each individual period. The optimal damping and smoothing factors that control the trade-off between fitting the data, model regularization and model smoothing were estimated at each period by the classic L-curve method (Rawlinson et al., 2006). Outliers with a traveltime residual beyond the 90% confidence level were removed after the first iteration. Figures 2 presents the inverted group velocity maps at selected periods after 10 iterations (see Figure S4 for the phase velocity maps, which exhibit similar patterns as in the group velocity maps). As can be seen, the most striking feature is low-velocity anomalies that fill the fore-arc CMB at most periods. The IBR in the west are featured by high-velocity anomalies at short periods but gradually become a low-velocity zone at periods exceeding 18 s. By contrast, high-velocity anomalies are commonly found beneath the back-arc CMB and the SP. We performed checkerboard tests to assess the resolution of the 2-D tomographic maps. The input model with anomaly size of 0.8° × 0.8° can be properly recovered at all periods (Figure S5). For the input anomaly size of 0.4° × 0.4°, we noticed that the smearing effects emerge at periods greater than 35 s in the back-arc CMB and the SP due to inadequate interstation ray coverage (Figure S6). Therefore, we focused only on large-scale structure in the uppermost mantle. We note that five permanent stations (KTA, KTN, NPW, SIM and TGI) that are located outside the well-resolved areas of the ambient noise tomographic maps were excluded from subsequent analysis.

2.2 P-wave receiver function analysis

RFs are sensitive to seismic discontinuities beneath the study region (Vinnik, 1977; Langston, 1979). We collected teleseismic events with magnitudes larger than 5.5 and epicentral distances of 30-90°. Most events are located to the east of Myanmar within the azimuthal range of 30-150° (Figure 3a). For RF calculation, three-component seismograms were zero-phase filtered to 0.01-4 Hz and trimmed to 20 s prior to and 100 s after the initial P-arrivals. Horizontal components were then rotated to the radial and tangential directions. Finally, radial RFs were generated by a time-domain maximum entropy deconvolution method (Wu et al., 2003) with a Gaussian parameter of 2.5 and water level of 0.001. We manually discarded incoherent RFs, such as those with anomalously long-period oscillation or with large coda amplitudes. The selection process yields a total of 13591 RFs.

We then prepared RF stacks at distributed grid nodes for joint inversion with surface wave dispersion. Some previous studies have attempted to suppress the potential effects of dipping interfaces or azimuthal anisotropy on the stacked RFs by narrowing the stacking range in both distance and back-azimuth (e.g., Wang et al., 2019) or stripping the RF back-azimuthal dependence via harmonic decomposition (e.g., Bianchi et al., 2010; Shen et al., 2012). However, such strategies are more suitable to resolve the 1-D velocity structure beneath a single station, where RF ray paths from other stations are not overlapping in the targeted depth range. The obtained single-station velocity models also require further interpolation to construct the final 3-D velocity model. Here our goal is to form laterally smoothed and continuous RF gathers throughout the study area. To that end, we employed the scheme proposed by Delph et al. (2015) to perform the RF common conversion point (CCP) stacking. Amplitudes on each RF were migrated along the ray path to the corresponding P-to-S conversion points using the global 1-D IASP91 model (Kennett and Engdahl, 1991). To match the grid spacing of dispersion data, we divided the study region into a grid of size 0.2° laterally by 0.5 km vertically and averaged all the amplitudes within a box-shaped cell centered at each grid node. The stacking cell has a minimum volume of 0.4°×0.4° laterally by 0.5 km vertically. We allowed the lateral cell width to expand in the step of 0.05° until 20 rays are included. It can be seen that the lateral cell width of 0.4° is sufficiently wide for most grid nodes at 30 km depth (Figure 3b). After the depth-domain stacking, RFs were transformed back to time using the IASP91 model again to minimize the effect of velocity model used on the resulting CCP stacked traces (Delph et al., 2015). The RFs can then be paired with Rayleigh wave dispersion curves at each grid node for joint inversion.

Figure 4 shows CCP stacked RFs at grid nodes along 22°N and 23°N. The RF waveforms exhibit clear variations from west to east. Whereas the P-to-S phases converted from the Moho show up consistently at 4-5 s east of 95°, it is difficult to trace the Moho signals continuously in the west. Compared to the linearly-stacked RFs produced independently at nearby stations, the primary phases are further enhanced in the CCP stacks but at the cost of slightly loss of RF amplitudes. Moreover, the sudden changes between RF stacks at neighboring stations, possibly caused by local structure variations, can be smoothed out through CCP stacking.

To better interpret the inverted shear velocity model, we also constructed two densely grid-spaced conventional CCP stacked profiles (e.g., Kind et al., 2002). Each profile was divided into cells with spatial intervals of 1 km along the profile and 0.5 km in depth. To take lateral velocity heterogeneity into account, we back-projected RF amplitudes along their ray paths in the new joint inversion model from this study (see section 3); below 80 km depth we assume the global 1-D IASP91 model for the back-projection (Kennett and Engdahl, 1991). All amplitudes that are in the same cell within a certain width on either side of the profile were stacked and normalized. The half-width of the stacking area was assigned as 40 km for the south profile and 80 km for the north one due to sparser data coverage in the north. A smoothing filter within one Fresnel zone was employed along the profile (e.g., a ~9.5 and ~14.5 km radius at 30 and 60 km depths, respectively). Considering the dipping feature of the subduction plate interfaces, for stations east of 95°E we confined RFs in the back-azimuthal range of 270°-360° and 0°-90° for CCP stacking (Zheng et al., 2020).

3. Inversion for shear velocity

A two-step inversion algorithm was adopted to determine the 1-D shear velocity model at individual geographical grid node. First, we applied the Markov chain Monte Carlo (McMC) transdimensional Bayesian approach (e.g., Bodin et al., 2012) in the implementation by Dreiling et al. (2020) to build a probabilistic model using only Rayleigh wave dispersion curves. Second, we refined the shear velocity model by performing an additional linear joint inversion which utilizes both dispersion data and RF waveforms (Herrmann, 2013). We prefer the two-step inversion strategy to a more direct one-step Bayesian joint inversion of both dispersion data and RFs because we found in initial tests, that the one-step inversion sometimes failed to find a simple model to simultaneously match dispersion and RF data. The two-step method can generally achieve better RF data fit, especially at nodes in the CMB where the RF wave trains are highly contaminated by sediment reverberations. Since our data are mostly sensitive to S-wave velocity, the corresponding P-wave velocity as well as density are set according to empirical relations (Birch, 1961; Brocher, 2005).

3.1 Bayesian inversion of Rayleigh wave dispersion

At each geographical grid node, we extracted Rayleigh wave group and phase velocity dispersion curves at 3-40 s period band from ambient noise tomography to build a 1-D shear velocity model. The 1-D model was described by a set of Voronoi nuclei (Bodin et al., 2012). The number of nuclei as well as their positions (i.e., depth and shear velocity) were treated as unknowns and arbitrarily drawn from uniform prior distributions during the inversion. A prior of 1-30 was assumed for the number of Voronoi nuclei, 0-80 km for the nucleus depth and 1.0-5.0 km/s for shear velocity.

The inverse problem was tackled in a Bayesian framework, where the complete solution is given by the *a posterior* probability distribution of the model $\mathbf{m}$ conditional on the observed data $\mathbf{d}_{obs}$, denoted by $p(\mathbf{m} \mid \mathbf{d}_{obs})$. Bayesian inference takes into account the *a prior* knowledge on the model $p(\mathbf{m})$ and the likelihood function $p(\mathbf{d}_{obs} \mid \mathbf{m})$ to express the posterior distribution function. The prior probability is considered as a product of independent uniform distributions on each model parameter, as defined in the previous paragraph. The likelihood term quantities the capability of a particular model to reproduce the observed data and can be written as

$$p(\mathbf{d}_{obs}|\mathbf{m}) = \frac{1}{\sqrt{(2\pi)^n|\mathbf{C}_e|}} \times \exp\left\{\frac{-\Phi(\mathbf{m})}{2}\right\} \quad (1)$$

$$\Phi(\mathbf{m}) = [g(\mathbf{m}) - \mathbf{d}_{obs}]^T \mathbf{C}_e^{-1} [g(\mathbf{m}) - \mathbf{d}_{obs}] \quad (2)$$

where the exponential term $\Phi(\mathbf{m})$ measures the disagreement between observed $\mathbf{d}_{obs}$ and predicted data $g(\mathbf{m})$, n is the size of data vector, i.e., the number of dispersion periods in our case, and $\mathbf{C}_e$ is the data covariance matrix accounting for the amplitude and correlation of data noise. It is noteworthy that the amplitude of data noise essentially determines the relative weighting between different data sets as well as model complexity. Following Bodin et al. (2012), we considered the noise amplitude as a non-model parameter to be varied from 0.0001 to 0.2 km/s in the inversion.

We performed the Monte Carlo search with 100 independent Markov chains. Each chain explores the model space 1.2 million times with the first 0.8 million iterations discarded as the burn-in phase. To avoid an unreasonable solution, we declared outlier chains that fail to reach the global plateau of the likelihood function as those with a median likelihood lower than 0.8

times the averagely-reached median of all chains. We further rejected any chains where the best-fitting model has a shear velocity of greater than 4.0 km/s in the top layer or that to be less than 3.0 km/s in the bottom half space. For 81% of all nodes, the number of outlier chains is no more than 10. Eventually, all the models after the burn-in phase from the non-outlier chains were thinned to an ensemble of 0.2 million samples whose density ought to follow the posterior distribution. We take the mean posterior model as a representative solution to the inverse problem. Figure S7 shows an example outcome of the Bayesian inversion.

3.2 Joint linear inversion of dispersion data and RFs

Rayleigh wave dispersion naturally provides tight constraints on the absolute shear velocity (Figure S8) but have broad sensitivity for the abrupt velocity contrasts over small depth ranges (e.g., Julià et al., 2000). Therefore, in the second step, we jointly inverted dispersion data with RFs through a linearized least-squares method in order to enhance the sensitivity to velocity interfaces (Julià et al., 2000; Herrmann, 2013). To reduce the dependence of linear inversion on the starting model, the data-driven probabilistic model from the Bayesian inversion was used at each node as initial input. The 1-D shear velocity structure is parameterized by a number of isotropic layers with constant thicknesses, i.e., 1 km in the top 30 km and 2 km at 30-80 km depths. We used Rayleigh wave dispersion values at 3-40 s period band and CCP stacked RF waveforms windowed at 5 s before and 15 s after the P-arrivals. The inversion was performed 40 times at each node with a damping value of 1 for the first 10 iterations and 0.2 for the following 30 iterations. The relative weighting between Rayleigh wave dispersion and RFs was assigned as 0.5, corresponding to equal contributions of both data sets to the inversion model.

4. Structure of the crust and uppermost mantle

Figure 5 shows final joint inversion results at four representative inversion nodes located in different tectonic units. Compared to the initial models derived only from surface wave dispersion data, the final inversion models retain the broad interstation structure captured by Rayleigh wave velocities while including the local sensitivity of RFs to the velocity interfaces.

More specifically, constraints from RF data sharpen the Moho discontinuity especially beneath the CMB and the SP, and introduce more details to the crustal structure. In Figure 5, the 1-D shear velocity structures differ considerably from each other at the four nodes. A low-velocity layer at 10-20 km depths can be distinguished at node N062 in the IBR (Figure 5a). A shear velocity of less than 2 km/s is observed in the upper crust under the fore-arc Chindwin basin (Figure 5b). In the uppermost mantle, a low-velocity zone at depths greater than 60 km is present beneath the back-arc Shwebo basin (Figure 5c). The shear velocity structure below the SP is rather simple, with a sharp Moho interface at ~35 km depth (Figure 5d). We note that the final inversion model can fit the observed data sets fairly well, except for RF waveforms associated with the fore-arc basin, where thick, low-velocity sediments may have a major impact on the observed RFs, and the local 1-D assumption underlying the inversions might no longer be appropriate (Figure 5b).

Figure 6 displays horizontal slices of the inverted 3-D shear velocity model at different depths. Beneath central Myanmar, the shear velocity structure exhibits obvious variations from the subsurface to the uppermost mantle. At a depth of 1 km, low-velocity anomalies (denoted by LV1) that represent the shallow sedimentary sequence occupy most area beneath the CMB, including the fore-arc Chindwin and back-arc Shwebo sub-basins. By contrast, relatively high-velocity anomalies can be seen beneath most of the IBR and the SP. At 5 km depth, while the Shwebo basin becomes less visible, the Chindwin basin shows up as prominent low-velocity anomalies (< 2.5 km/s, LV1), which are well sandwiched between the Kabaw fault in the west and the Wuntho-Popa magmatic arc in the east. The thick, low-velocity sediments can be directly inferred from the observed data, e.g., slow surface wave propagation (< 2 km/s) in the ambient noise data (Figures 5b, S1 and S2) and complicated first peaks in the RFs (Figure 4). The crustal structure at shallow depths overall correlates well with surface geology but varies with increasing depth. At 12 km depth, low-velocity anomalies still dominate the fore-arc basin but appear more pronounced in the north. To the west of the CMB, a second low-velocity zone (LV2) emerges from the southern IBR and then expands to the entire orogenic belts at 20 km depth, with shear velocity exceeding 3.5 km/s (renamed as LV3) from 30 km downwards.

Conversely, the low-velocity anomalies below the fore-arc basin gradually give way to high-velocity anomalies. At a depth of 40 km, localized low-velocity anomalies (LV4) are imaged roughly below the Holocene Monywa volcano. Down to a depth of 50 km, the IBR are still characterized by low-velocity anomalies. By contrast, the fore-arc basin is featured by high-velocity anomalies relative to the rest of the study region. Shear velocity values as high as 4.5 km/s reflect upper mantle material at this depth. A clear division between a fast western part and a slower eastern part of the study region appears at 78 km depth. Low-velocity anomalies (LV5) spread out beneath the back-arc area.

Two vertical Vs cross sections that transect the main tectonic units are shown in Figures 7a and 8a, with their corresponding locations given in Figure 6a. In both profiles, low-velocity anomalies of less than 2.5 km/s (LV1) dominate the shallowmost crust beneath the CMB. The thickness of the fore-arc Chindwin basin varies from ~8 km in the south profile (AA') to ~18 km in the north one (BB'). The fore-arc basin is evidently thicker than the back-arc basin. A clear decrease in the sedimentary thickness at ~95°E, from over 8 km in the western fore-arc CMB to less than 3 km in the eastern back-arc region, matches well with the surface location of the magmatic arc. In the mid-lower crust, the IBR are featured by low-velocity anomalies of less than 3.3 km/s (LV2), which are more noticeable at 10-20 km depths along profile AA'. At a depth range of 30-40 km, the sharp velocity variation from ~3.8 to ~4.2 km/s depicts the Moho interface. The Moho in the shear velocity model is defined at the depth where the vertical velocity gradient reaches a local maximum between 3.5 and 4.5 km/s. Beneath the CMB and the SP, our joint inversion results reveal a relatively flat Moho that generally follows the 4.0 km/s velocity isoline, and the average Moho depth is ~30 and ~35 km along profiles AA' and BB', respectively. It is noteworthy that the Moho is clearly interrupted at the place where LV4 appears. Beneath the IBR, it is difficult to delineate the Moho of the overriding Burma plate due to the presence of the subduction zone. At a depth range of 25-55 km below the IBR, low-velocity anomalies (LV3) dipping with a gentle angle to the east correlate well with a focused and also east-dipping set of intermediate-depth seismicity. This low-velocity zone is clearly discriminated from underlying mantle of shear velocity faster than 4.5 km/s. Beneath the back-arc CMB, another upper mantle low-velocity body (LV5) can be distinguished at depths greater than 55 km. Along profile AA', this low-velocity zone tends to extend upwards and connect to LV4 at the base of the crust. By contrast, the fore-arc region is featured by relatively high-velocity upper mantle material. Along the same profiles, Figure S9 displays the surface wave only Bayesian inversion model, which overall exhibits similar velocities but a less clear Burma Moho, compared to the final joint inversion model (Figures 7a and 8a).

To assist in discontinuity interpretation, we also perform conventional CCP stacking, with denser grid spacing than used for joint inversion, along the two profiles (Figures 7b and 8b). The Ps delay time is corrected for 3-D velocity heterogeneity by the joint inversion model. Overall, features presented in the CCP stacked profiles are compatible with those in the shear velocity model. The thickness contrast between the fore-arc and the back-arc basins is confirmed by the CCP stacked profiles. The Moho topography obtained by CCP stacking shows more details than that in the joint inversion results. Along profile AA', the continuity of the Burma Moho is truncated at two locations. The gap in the Moho at 94.5-95°E coincides with the place where the upper mantle LV4 interacts with the base of the crust. Another Moho gap is found at ~96°E, roughly below the dextral Sagaing fault. We think that this Moho gap may not reflect the currently active Sagaing fault but represent an older suture because it is not consistent with the distribution of the crustal earthquakes occurring along the fault near ~22°N. Such hypothesis is supported by the observed outcrop of Mogok metamorphic belt west of the Sagaing fault between Mandalay and Shwebo (Lothar Ratschbacher, personal communication; Myanmar Geosciences Society, 2014). These metamorphic rocks are thought to originate at depth in the mid-lower crust during the Tertiary, which is prior to the dextral motion on the Sagaing fault (Searle et al., 2007). Along profile BB', the Moho is continuous below the CMB and the SP without any visible disconnection. Nevertheless, we notice that the Moho depth elevates from ~40 km beneath the fore-arc to ~30 km beneath the back-arc region, and then deepens back to ~40 km beneath the SP. In addition, two subparallel Ps phases, with a negative phase above a positive one, are well imaged at depths of ~25-90 km in the western part of profile AA'. The upper negative phase runs from ~25 km to 60 km depth while the lower positive phase extends from ~45 km to depths greater than 80 km. These two phases with a dip of ~20° towards the east envelop most of the intermediate-depth earthquakes. Along profile BB', an east-dipping negative phase can be observed at ~40-65 km depths while no dipping positive phase is distinguishable at greater depths.

5. Discussion

5.1 Basin structure

Seismic velocity structure beneath the CMB has been previously investigated by active source seismic surveys, but only along several short profiles (Pivnik et al., 1998; Bertrand and Rangin, 2003). Wang et al. (2019) also provide shear velocity structure under discrete seismic stations in the CMB. Unfortunately, only six of their stations are located in our study region. With improved shallow sensitivity especially from ambient noise derived Rayleigh wave velocity dispersion (e.g., Figure S8), we are able to constrain the basin structure of central Myanmar on a regional scale.

In our joint inversion results, the most prominent feature in the upper crust is LV1 of less than 2.5 km/s beneath the fore-arc Chindwin sub-basin. Geologically, the Chindwin basin lies completely in the fore-arc domain and comprises both marine and non-marine deposits (Ridd and Racey, 2015). This basin is bounded by the IBR in the west and the magmatic arc in the east, as verified by both ambient noise tomography and joint shear velocity inversion results (Figures 2 and 6). In the south, the Chindwin basin is separated with the Minbu basin by a small topographic high at ~22°N. In the north it extends beyond our study region to ~26°N (Bender, 1983; Pivnik et al., 1998). Our joint inversion model clearly shows that the sedimentary thickness of the Chindwin basin gradually increases northwards from ~8 km at its southern edge (~22°N) to a maximum value of 18 km at the depocenter (~23°N) (Figures 6-8). The remarkably-thick Chindwin basin and its thickening trend towards the north is echoed by the Bouguer gravity map, showing strong negative anomaly in the fore-arc region with a minimum value of -175 mGal at ~23°N. (Mukhopadhyay and Dasgupta, 1988; Pivnik et al., 1998). With sparser data distribution than ours, recent ambient noise tomography study for almost the entire Myanmar region also suggests two distinct depocenters, located in the Chindwin and the Minbu basins (Wu et al., 2021).

Across the magmatic arc, the sedimentary thickness abruptly decreases from over 8 km in the fore-arc Chindwin basin to less than 3 km immediately east of it in the back-arc Shwebo basin (Figures 7 and 8). This thickness contrast agrees well with existing observations in the adjacent region (Bertrand and Rangin, 2003; Wu et al., 2021; Zhang et al., 2021), although the exact sedimentary thickness probed by different studies varies slightly. The fore-arc/back-arc differentiation could be related to the obliquely-eastward subduction of the Indian plate. Until the mid-Eocene time, the Burma subduction margin was still dominated by the subduction of the Neotethyan oceanic plate and acted as a typical Andean-type setting, with the CMB as a whole situating in the fore-arc domain open to the trench (Licht et al., 2018). The basin floor at that time was dipping seawards (i.e., westwards) and more sediments were deposited closer to the trench. Since the late Eocene, following the onset of oblique subduction of India relative to Eurasia, the present-day IBR began emerging and served as an offshore barrier, trapping sediments in the CMB. Simultaneously, modern fore-arc/back-arc setting of the CMB was established as the active Wuntho-Popa arc developed at the central axis of the CMB (Licht et al., 2018; Zhang et al., 2018). The fore-arc basin, formerly closer to the trench, should have greater accommodation space and thus be able to trap more deposits than the back-arc basin. This scenario could explain a thick fore-arc basin and a much thinner back-arc basin in our joint inversion model. Than (2014) ascribes the thickness contrast between the fore-arc and back-arc basins to different types of underlying basement material. Whilst the fore-arc basin is underlain by dense oceanic crust, the back-arc basin is floored by lighter continental crust. However, Rangin et al. (2013) infer the main crustal suture lying farther west. In addition, both our new results and Wang et al. (2019) suggest an average Moho depth beneath the whole CMB to be ~30 km, standing for continental crust.

5.2 Slow mid-lower crust in the IBR

Below the IBR, we observe low-velocity anomaly LV2 with shear velocities less than 3.3 km/s in the middle to lower crust. This crustal low-velocity zone is more noticeable in the south than in the north profile. We performed additional ambient noise tomography using dispersion measurements from sparser stations selected along the linear array ~22°N and obtained similar results (Figure S10), thus verified that the northward weakening of LV2 is not an artifact due to uneven distribution of seismic stations. Similarly, recent tomographic images, either produced using ambient noise or local earthquake data, also reveals low-velocity anomalies at depths shallower than 30 km beneath the IBR (Raoof et al., 2017; Wu et al., 2021; Zhang et al., 2021). It is commonly observed that low-velocity zones dominate the fore-arc structure atop the incoming subducted plates (e.g., Calvert et al., 2011; Scarfì et al., 2018). This signature is generally attributed to weak and aseismic sedimentary material being scraped off the downgoing slab at the trench followed by accretion to the toe of the upper plate (e.g., Byrne et al., 1988). West of the IBR, a thick (>15 km) layer of sedimentary rocks covering the Bengal basin has been reported by recent studies (e.g., Singh et al., 2016; Mitra et al., 2018). It can thus be inferred that a great quantity of sediments may have accompanied the Indian crust into the subduction zone (Steckler et al., 2016). The majority of buoyant sediment material could not penetrate deeper into the mantle, but detach from the underlying Indian crust and contribute to the growth of the accretionary prism. Some of the sediments might have also subducted and recycled to the Burma crust by magmatism, as implied by enriched Nd-Sr isotropic composition of the magmatic rocks through time (Licht et al., 2020). We note that the eastern portion of the IBR resolved by this study belongs to the inner accretionary prism, which is primarily made of a high-grade metamorphic core (e.g., Bender, 1983; Maurin and Rangin, 2009; Licht et al., 2018; Morley et al., 2020). Former laboratory study suggests that the shear velocity of typical metamorphic rocks in the mid-lower crust ranges from 3.1 to 3.7 km/s (Christensen, 1966), which is generally in line with the shear velocity of LV2 along profile BB' but is slightly higher than what we observe along profile AA'. Changes in velocity of LV2 could be attributed to varying seismic properties in accreted material. We suspect that the accreted sediments of the inner wedge may possibly experience lower degree of consolidation and/or metamorphism south of 23°N. These much weaker and fluid-richer material might cause a slower LV2 along profile AA' than profile BB', as in the joint inversion results (Figures 7 and 8). However, detailed information on the crustal Vp/Vs ratio under the IBR is needed to clarify this speculation.

5.3 Eastward subduction of the Indian crust

Previous teleseismic tomographic studies interpret the upper mantle high-velocity anomaly, with a steep angle diving towards the east beneath Myanmar, as the subducted Indian plate (e.g., Li et al., 2008; Pesicek et al., 2010; Koulakov, 2011; Yao et al., 2021). However, the geometry of the subducted slab at shallow depths is hampered due to scarcity of seismic stations in Myanmar. In our joint inversion model, anomaly LV3 with shear velocity less than 4.2 km/s and a thickness of ~25 km likely represents the crustal rocks subducted to a depth of 55 km beneath the IBR (Figures 7a and 8a). Below this depth, the low-velocity zone tends to vanish, even though the seismic Benioff zone show clear signs that the subducted slab has extended to at least 80 km depth. The simplest explanation for the fading of the slab signature at depths greater than 55 km is that the upper mantle velocity structure beneath the fore-arc region might not be well constrained by joint inversion, probably due to the existence of a thick sedimentary cover, resulting in poor RF data fit and reduced resolving power of surface wave dispersion in the upper mantle (e.g., Figures 5b and S8). Alternatively, the apparent termination of the low-velocity zone at depth may be due to the partially eclogitization of the subducted crust (e.g., Zhang et al., 2021). The bulk density of continental crust can be significantly increased by eclogitization (Krystopowicz and Currie, 2013), which would result in pronounced reduction in the velocity contrast with the ambient mantle. Given that the sharp Ps phases from the slab boundaries are clearly imaged by RFs (Figure 7b and Zheng et al., 2020), we discuss more on the CCP stacked profiles.

Along profile AA', two subparallel east-trending Ps phases, with the negative phase above the positive one, suggest the existence of a low-velocity layer with an average thickness of ~25 km below the IBR and the fore-arc Chindwin basin (Figure 7b). This observation is in agreement with LV3 in the joint inversion profile (Figure 7a). Following Zheng et al. (2020), we interpret such thick low-velocity layer that hosts most of the intermediate-depth seismicity as the subducted Indian continental crust. The upper and lower boundaries of the subducted crust are less obvious along profile BB'. Nevertheless, beneath the Chindwin basin a negative signal with a dip angle of ~22° towards the east is found at a similar depth range where the top slab interface along profile AA' is positioned (Figures 7b and 8b). We further assessed the back-azimuthal variation in RF phases for two representative stations that are located directly above this negative phase. Consequently, a negative Ps phase at ~10 s shows a roughly 360° periodic change in back-azimuth for both stations, which is comparable to the azimuthal periodicity of a Ps phase converted from a predefined east-dipping interface with downward velocity decrease (Figure S11). These tests suggest that this negative RF phase below the Burma Moho could represent the top interface of the subducted Indian crust. We suspect that the upward extent of the negative signals into LV2 below the IBR in both profiles (dotted lines in Figures 7 and 8) may not reflect the slab interface but indicate the complexity of crustal structure atop the subducted plate, as proposed by Zheng et al. (2020). Below 60 km depth, no continuous positive signal can be traced in the CCP stacked profile along BB'. However, if we assume that intermediate depth seismicity normally occurs at the mid-lower Indian crust, as implied from the south profile along AA', the inferred thickness of the subducted crust, that is the depth interval between the east-dipping negative Ps phase and the deep limit of the seismogenic zone, could be more than 20 km.

CCP stacking also suggests contrast features atop the upper slab interface along profiles AA' and BB'. In the north, the overlying Burma Moho of 35-40 km depths beneath the Chindwin basin is characterized by strong amplitudes and tend to bend towards the downgoing Indian crust (Figure 8b). This feature is different from the Burma Moho in the south, where the Moho moves sub-horizontally at 30-35 km depths (Figure 7b). In addition, along BB' an earthquake cluster, closely following the dip trend of the subducted slab, is positioned at depths greater than ~20 km in the Burma crust. Earthquakes within this seismic zone show thrusting focal mechanisms, indicative of a compressive regime. It is worth noting that no earthquake cluster is observed at the base of the Burma crust along profile AA'. The lower-crustal seismic zone, together with the bending feature of the Burma Moho, hints at a different state of stress at the plate boundary along ~23°N from that along ~22°N.

5.4 Upper mantle low-velocity material below the CMB

Beneath the CMB, upper mantle low-velocity anomalies of shear velocity less than 4 km/s are observable at depths greater than 35 km between ~94.5° and ~96°E (Figures 6-8). More specifically, small-scale LV4 is found under the Burma crust within ~94.5-95°E and ~21.5-22.5°N, immediately below the Monywa volcano. This feature is echoed by a Moho gap in the CCP stacked profile at a similar position. Whilst LV4 only shows up in the southern study region, another upper mantle low-velocity body LV5 occupies almost the entire back-arc domain at the base of the joint inversion model. Other recent seismological studies also observed low velocities in the mantle wedge of the Indo-Burma subduction zone (Zheng et al., 2020; Wu et al., 2021; Zhang et al., 2021). Zheng et al. (2020) interpret LV4 as a deep arc magma chamber formed by partial melting of the mantle wedge, which was rehydrated by fluids released by dehydration of the subducted Indian slab. An earlier magnetotelluric survey along ~22°N reveals a low resistivity anomaly at a similar position as LV4, which is also thought to be linked to subduction-induced fluids (Rao et al., 2014). We discover a potential connection of LV5 to LV4 in the shallowmost mantle along profile AA' (Figure 7a). We suspect that this low-velocity mantle upwelling might possibly ascend farther to the subsurface and promote the Monywa volcanism in the recent times (Lee et al., 2016). By contrast, LV5 remains largely at depths greater than 60 km in the north profile, correspondingly no volcano appears on the surface at ~23°N. Although slab dehydration is commonly invoked to interpret the low-velocity anomalies in the mantle wedge, recent geochemical analyses suggest that the volcanism during the latest Quaternary stage is compositionally more heterogeneous, which can hardly be explained by slab dehydration alone but requires additional contribution of partial melting from the asthenosphere (Lee et al., 2016; Zhang et al., 2020). Our joint inversion results show strong indication of low-velocity zones in the uppermost mantle beneath the CMB, but further effort, e.g., joint regional and teleseismic tomography aiming at a broader depth range with more seismic data is required to determine their origins.

6. Conclusion

Using continuous and teleseismic data retrieved at 79 broadband seismic stations, we obtain new 3-D shear velocity images beneath central Myanmar by joint inversion of Rayleigh wave dispersion and CCP-derived RFs. We also construct two traditional CCP stacked profiles using the new joint inversion model. Our results display clear variations in both shear velocity and seismic discontinuity across the study region (Figure 9).

Basin structure is well constrained by joint inversion. Low shear velocity values of less than 2.5 km/s dominate the near-surface structure under the CMB, standing for unconsolidated sediments. In the fore-arc Chindwin basin, sedimentary rocks possess low-velocity speeds in the range of ~1.5-2.5 km/s and a north-dipping basement of ~8-18 km depths. The sedimentary basement elevates abruptly to a depth of less than 3 km across the Wuntho-Popa magmatic arc into the Shwebo basin. Depth variations of the sedimentary basement in the joint inversion model agree with those inferred by CCP stacking. Seismic structure beneath the IBR is complicated. Low velocity anomalies (< 3.3 km/s) in the top 20 km may represent the inner accretionary prism, which is more prominent in the south (at 22°N) than in the north (at 23°N). The eastward subducted crust of the Indian plate is characterized by low velocities with a thickness of ~25 km down to a depth of ~60 km. This east-trending low-velocity layer might not be well resolved at greater depths beneath the CMB. Along profile BB', we infer the negative RF phase with an east-dipping angle of ~22° at ~40-60 km depths as the upper slab interface, comparable to what we observed along AA'. The Moho interface of the overriding Burma plate is located at 30-40 km depths, showing clear depth variations and gaps. In the uppermost mantle, low-velocity anomalies (< 4 km/s) appear at depths greater than 60 km beneath the majority of the back-arc region, which might possibly represent a fluid- or melt-rich channel caused by subduction dehydration and/or asthenospheric upwelling.

Acknowledgement

Seismic waveform data were provided by Seismic Array Laboratory at the Institute of Geology and Geophysics, Chinese Academy of Sciences (IGGCAS) (http://doi.org/10.12129/IGGSL.Data.Observation), the Incorporated Research Institutions for Seismology (IRIS) (https://doi.org/10.7914/SN/MM) and the GEOFON Data Center (https://doi.org/10.14470/TR560404). We are grateful to all the participants for installing and maintaining the CMGSMO seismic network. We thank Lothar Ratschbacher, Bernd Schurr, Timm John, Sascha Zertani, Ji'en Zhang, Xin Wang, Tianyu Zheng for valuable discussion, Yuan Ling, Ying Chen for technical assistance and Xingli Fan for sharing the ambient noise data processing code. The Bayesian inversion were implemented by the BayHunter package (Dreiling and Tilmann, 2019). The Computer Programs in Seismology (NP330) software was used to perform joint linearized least-squares inversion (Herrmann, 2013). We computed synthetic seismograms using the RAYSUM code (Frederiksen and Bostock, 2000), which accounts for dipping interfaces. Figures were generated by the Generic Mapping Tools (GMT) (Wessel et al., 2013). This study is supported by National Natural Science Foundation of China (grants 91755214, 42030309 and 41490612), the Strategic Priority Research Program (B) of Chinese Academy of Sciences (XDB18000000) and the International Partnership Program of the Chinese Academy of Sciences (GJHZ1776). Y. B. is partially funded by China Scholarship Council (201804910411). We thank two anonymous reviewers for helpful comments, which helped to improve the presentation of our results.

References

Bai, Y., Yuan, X., He, Y., Hou, G., Thant, M., Sein, K., Ai, Y., 2020. Mantle Transition Zone Structure Beneath Myanmar and Its Geodynamic Implications. Geochemistry, Geophysics, Geosystems 21, e2020GC009262. 10.1029/2020GC009262

Bender, F., 1983. Geology of Burma. Gebrüder Borntraeger, Berlin, Stuttgart.

Bensen, G.D., Ritzwoller, M.H., Barmin, M.P., Levshin, A.L., Lin, F., Moschetti, M.P., Shapiro, N.M., Yang, Y., 2007. Processing seismic ambient noise data to obtain reliable broad-band surface wave dispersion measurements. Geophysical Journal International 169, 1239-1260. 10.1111/j.1365-246X.2007.03374.x

Bertrand, G., Rangin, C., 2003. Tectonics of the western margin of the Shan plateau (central Myanmar): implication for the India–Indochina oblique convergence since the Oligocene. Journal of Asian Earth Sciences 21, 1139-1157. 10.1016/S1367-9120(02)00183-9

Bianchi, I., Park, J., Piana Agostinetti, N., Levin, V., 2010. Mapping seismic anisotropy using harmonic decomposition of receiver functions: An application to Northern Apennines, Italy. Journal of Geophysical Research: Solid Earth 115. 10.1029/2009jb007061

Birch, F., 1961. The velocity of compressional waves in rocks to 10 kilobars: 2. Journal of Geophysical Research (1896-1977) 66, 2199-2224. 10.1029/JZ066i007p02199

Bodin, T., Sambridge, M., Gallagher, K., Rawlinson, N., 2012. Transdimensional inversion of receiver functions and surface wave dispersion. Journal of Geophysical Research: Solid Earth 117. 10.1029/2011jb008560

Borcherdt, R.D., Gibbs, J.F., 1976. Effects of local geological conditions in the San Francisco Bay region on ground motions and the intensities of the 1906 earthquake. Bulletin of the Seismological Society of America 66, 467-500.

Brocher, T.M., 2005. Empirical Relations between Elastic Wavespeeds and Density in the Earth's Crust. Bulletin of the Seismological Society of America 95, 2081-2092. 10.1785/0120050077

Byrne, D.E., Davis, D.M., Sykes, L.R., 1988. Loci and maximum size of thrust earthquakes and the mechanics of the shallow region of subduction zones. Tectonics 7, 833-857. 10.1029/TC007i004p00833

Calvert, A.J., Preston, L.A., Farahbod, A.M., 2011. Sedimentary underplating at the Cascadia mantle-wedge corner revealed by seismic imaging. Nature Geoscience 4, 545-548. 10.1038/ngeo1195

Christensen, N.I., 1966. Shear wave velocities in metamorphic rocks at pressures to 10 kilobars. Journal of Geophysical Research (1896-1977) 71, 3549-3556. 10.1029/JZ071i014p03549

Delph, J.R., Zandt, G., Beck, S.L., 2015. A new approach to obtaining a 3D shear wave velocity model of the crust and upper mantle: An application to eastern Turkey. Tectonophysics 665, 92-100. 10.1016/j.tecto.2015.09.031

Dreiling, J., Tilmann, F., 2019. BayHunter - McMC transdimensional Bayesian inversion of receiver functions and surface wave dispersion. GFZ Data Services. 10.5880/GFZ.2.4.2019.001

Dreiling, J., Tilmann, F., Yuan, X., Haberland, C., Seneviratne, S.W.M., 2020. Crustal Structure of Sri Lanka Derived From Joint Inversion of Surface Wave Dispersion and Receiver

Functions Using a Bayesian Approach. Journal of Geophysical Research: Solid Earth 125, e2019JB018688. 10.1029/2019JB018688

Engdahl, E.R., Di Giacomo, D., Sakarya, B., Gkarlaouni, C.G., Harris, J., Storchak, D.A., 2020. ISC-EHB 1964–2016, an Improved Data Set for Studies of Earth Structure and Global Seismicity. Earth and Space Science 7, e2019EA000897. 10.1029/2019ea000897

Frederiksen, A.W., Bostock, M.G., 2000. Modelling teleseismic waves in dipping anisotropic structures. Geophysical Journal International 141, 401-412. 10.1046/j.1365-246x.2000.00090.x

Gripp, A.E., Gordon, R.G., 2002. Young tracks of hotspots and current plate velocities. Geophysical Journal International 150, 321-361. 10.1046/j.1365-246X.2002.01627.x

Herrmann, R.B., 2013. Computer Programs in Seismology: An Evolving Tool for Instruction and Research. Seismological Research Letters 84, 1081-1088. 10.1785/0220110096

Hurukawa, N., Maung Maung, P., 2011. Two seismic gaps on the Sagaing Fault, Myanmar, derived from relocation of historical earthquakes since 1918. Geophysical Research Letters 38. 10.1029/2010gl046099

Hurukawa, N., Tun, P.P., Shibazaki, B., 2012. Detailed geometry of the subducting Indian Plate beneath the Burma Plate and subcrustal seismicity in the Burma Plate derived from joint hypocenter relocation. Earth, Planets and Space 64, 333-343. 10.5047/eps.2011.10.011

Julià, J., Ammon, C.J., Herrmann, R.B., Correig, A.M., 2000. Joint inversion of receiver function and surface wave dispersion observations. Geophysical Journal International 143, 99-112. 10.1046/j.1365-246x.2000.00217.x

Kennett, B.L.N., Engdahl, E.R., 1991. Traveltimes for global earthquake location and phase identification. Geophysical Journal International 105, 429-465. 10.1111/j.1365-246X.1991.tb06724.x

Kind, R., Yuan, X., Saul, J., Nelson, D., Sobolev, S.V., Mechie, J., Zhao, W., Kosarev, G., Ni, J., Achauer, U., Jiang, M., 2002. Seismic images of crust and upper mantle beneath Tibet: evidence for Eurasian plate subduction. Science 298, 1219-1221. 10.1126/science.1078115

Koulakov, I., 2011. High-frequency P and S velocity anomalies in the upper mantle beneath Asia from inversion of worldwide traveltime data. Journal of Geophysical Research 116, B04301. 10.1029/2010JB007938

Krystopowicz, N.J., Currie, C.A., 2013. Crustal eclogitization and lithosphere delamination in orogens. Earth and Planetary Science Letters 361, 195-207. 10.1016/j.epsl.2012.09.056

Kumar, A., Mitra, S., Suresh, G., 2015. Seismotectonics of the eastern Himalayan and indo-burman plate boundary systems. Tectonics 34, 2279-2295. 10.1002/2015tc003979

Langston, C.A., 1979. Structure under Mount Rainier, Washington, inferred from teleseismic body waves. Journal of Geophysical Research: Solid Earth 84, 4749-4762. 10.1029/JB084iB09p04749

Lee, H.-Y., Chung, S.-L., Yang, H.-M., 2016. Late Cenozoic volcanism in central Myanmar: Geochemical characteristics and geodynamic significance. Lithos 245, 174-190. 10.1016/j.lithos.2015.09.018

Li, C., van der Hilst, R.D., Meltzer, A.S., Engdahl, E.R., 2008. Subduction of the Indian lithosphere beneath the Tibetan Plateau and Burma. Earth and Planetary Science Letters 274, 157-168. 10.1016/j.epsl.2008.07.016

Licht, A., Dupont-Nivet, G., Win, Z., Swe, H.H., Kaythi, M., Roperch, P., Ugrai, T., Littell, V., Park, D., Westerweel, J., Jones, D., Poblete, F., Aung, D.W., Huang, H., Hoorn, C., Sein, K., 2018. Paleogene evolution of the Burmese forearc basin and implications for the history of India-Asia convergence. GSA Bulletin 131, 730-748. 10.1130/b35002.1

Licht, A., Win, Z., Westerweel, J., Cogné, N., Morley, C.K., Chantraprasert, S., Poblete, F., Ugrai, T., Nelson, B., Aung, D.W., Dupont-Nivet, G., 2020. Magmatic history of central Myanmar and implications for the evolution of the Burma Terrane. Gondwana Research 87, 303-319. 10.1016/j.gr.2020.06.016

Maurin, T., Rangin, C., 2009. Structure and kinematics of the Indo-Burmese Wedge: Recent and fast growth of the outer wedge. Tectonics 28, TC2010. 10.1029/2008TC002276

Metcalfe, I., 2011. Tectonic framework and Phanerozoic evolution of Sundaland. Gondwana Research 19, 3-21. doi.org/10.1016/j.gr.2010.02.016

Mitchell, A.H.G., 1993. Cretaceous–Cenozoic tectonic events in the western Myanmar (Burma)–Assam region. Journal of the Geological Society 150, 1089-1102. 10.1144/gsjgs.150.6.1089

Mitra, S., Priestley, K.F., Borah, K., Gaur, V.K., 2018. Crustal Structure and Evolution of the Eastern Himalayan Plate Boundary System, Northeast India. Journal of Geophysical Research: Solid Earth 123, 621-640. 10.1002/2017jb014714

Molnar, P., Stock, J.M., 2009. Slowing of India's convergence with Eurasia since 20 Ma and its implications for Tibetan mantle dynamics. Tectonics 28, TC3001. 10.1029/2008TC002271

Mon, C.T., Gong, X., Wen, Y., Jiang, M., Chen, Q.-F., Zhang, M., Hou, G., Thant, M., Sein, K., He, Y., 2020. Insight Into Major Active Faults in Central Myanmar and the Related Geodynamic Sources. Geophysical Research Letters 47, e2019GL086236. 10.1029/2019gl086236

Morley, C.K., Tin Tin, N., Searle, M., Robinson, S.A., 2020. Structural and tectonic development of the Indo-Burma ranges. Earth-Science Reviews 200, 102992.

10.1016/j.earscirev.2019.102992

Mukhopadhyay, M., Dasgupta, S., 1988. Deep structure and tectonics of the burmese arc: constraints from earthquake and gravity data. Tectonophysics 149, 299-322. 10.1016/0040-1951(88)90180-1

Myanmar Geosciences Society, 2014. Geological Map of Myanmar, 1:2 250 000 scale. Myanmar Geosciences Society, Yangon, Myanmar.

Ni, J.F., Guzman-Speziale, M., Bevis, M., Holt, W.E., Wallace, T.C., Seager, W.R., 1989. Accretionary tectonics of Burma and the three-dimensional geometry of the Burma subduction zone. Geology 17, 68-71. 10.1130/0091-7613(1989)017<0068:ATOBAT>2.3.CO;2

Pesicek, J.D., Thurber, C.H., Widiyantoro, S., Zhang, H., DeShon, H.R., Engdahl, E.R., 2010. Sharpening the tomographic image of the subducting slab below Sumatra, the Andaman Islands and Burma. Geophysical Journal International 182, 433-453. 10.1111/j.1365-246X.2010.04630.x

Pivnik, D.A., Nahm, J., Tucker, R.S., Smith, G.O., Nyein, K., Nyunt, M., Maung, P.H., 1998. Polyphase Deformation in a Fore-Arc/Back-Arc Basin, Salin Subbasin, Myanmar (Burma)1. AAPG Bulletin 82, 1837-1856. 10.1306/1d9bd15f-172d-11d7-8645000102c1865d

Rangin, C., Maurin, T., Masson, F., 2013. Combined effects of Eurasia/Sunda oblique convergence and East-Tibetan crustal flow on the active tectonics of Burma. Journal of Asian Earth Sciences 76, 185-194. 10.1016/j.jseaes.2013.05.018

Rao, C.K., Selvaraj, C., Gokarn, S.G., 2014. Deep electrical structure over the igneous arc of the Indo Burman Orogen in Sagaing province, Myanmar from magnetotelluric studies. Journal of Asian Earth Sciences 94, 68-76. 10.1016/j.jseaes.2014.08.016

Raoof, J., Mukhopadhyay, S., Koulakov, I., Kayal, J.R., 2017. 3-D seismic tomography of the lithosphere and its geodynamic implications beneath the northeast India region. Tectonics 36, 962-980. 10.1002/2016tc004375

Rawlinson, N., Reading, A.M., Kennett, B.L.N., 2006. Lithospheric structure of Tasmania from a novel form of teleseismic tomography. Journal of Geophysical Research: Solid Earth 111. 10.1029/2005JB003803

Rawlinson, N., Sambridge, M., 2005. The Fast Marching Method: An Effective Tool for Tomographic Imaging and Tracking Multiple Phases in Complex Layered Media. Exploration Geophysics 36, 341-350. 10.1071/EG05341

Ridd, M.F., Racey, A., 2015. Chapter 4 Onshore petroleum geology of Myanmar: Central Burma Depression. Geological Society, London, Memoirs 45, 21-50. 10.1144/m45.04

Satyabala, S.P., 2003. Oblique Plate Convergence in the Indo-Burma (Myanmar) Subduction

Region. pure and applied geophysics 160, 1611-1650. 10.1007/s00024-003-2378-0

Scarfì, L., Barberi, G., Barreca, G., Cannavò, F., Koulakov, I., Patanè, D., 2018. Slab narrowing in the Central Mediterranean: the Calabro-Ionian subduction zone as imaged by high resolution seismic tomography. Scientific Reports 8, 5178. 10.1038/s41598-018-23543-8

Searle, M.P., Noble, S.R., Cottle, J.M., Waters, D.J., Mitchell, A.H.G., Hlaing, T., Horstwood, M.S.A., 2007. Tectonic evolution of the Mogok metamorphic belt, Burma (Myanmar) constrained by U-Th-Pb dating of metamorphic and magmatic rocks. Tectonics 26. 10.1029/2006TC002083

Shapiro, N.M., Campillo, M., 2004. Emergence of broadband Rayleigh waves from correlations of the ambient seismic noise. Geophysical Research Letters 31. 10.1029/2004GL019491

Shapiro, N.M., Campillo, M., Stehly, L., Ritzwoller, M.H., 2005. High-Resolution Surface-Wave Tomography from Ambient Seismic Noise. Science 307, 1615-1618. 10.1126/science.1108339

Shen, W., Ritzwoller, M.H., Schulte-Pelkum, V., Lin, F.-C., 2012. Joint inversion of surface wave dispersion and receiver functions: a Bayesian Monte-Carlo approach. Geophysical Journal International 192, 807-836. 10.1093/gji/ggs050

Singh, A., Bhushan, K., Singh, C., Steckler, M.S., Akhter, S.H., Seeber, L., Kim, W.-Y., Tiwari, A.K., Biswas, R., 2016. Crustal structure and tectonics of Bangladesh: New constraints from inversion of receiver functions. Tectonophysics 680, 99-112. 10.1016/j.tecto.2016.04.046

Steckler, M.S., Mondal, D.R., Akhter, S.H., Seeber, L., Feng, L., Gale, J., Hill, E.M., Howe, M., 2016. Locked and loading megathrust linked to active subduction beneath the Indo-Burman Ranges. Nature Geoscience 9, 615-618. 10.1038/ngeo2760

Taylor, M., Yin, A., 2009. Active structures of the Himalayan-Tibetan orogen and their relationships to earthquake distribution, contemporary strain field, and Cenozoic volcanism. Geosphere 5, 199-214. 10.1130/GES00217.1

Than, N.M., 2014. Tectonic controls on Central Myanmar Basin (CMB) development and hydrocarbon occurrences (abstract only). American Association of Petroleum Geologists, Myanmar Geosciences Society Conference, 14–15 August.

Vinnik, L.P., 1977. Detection of waves converted from P to SV in the mantle. Physics of the Earth and Planetary Interiors 15, 39-45. 10.1016/0031-9201(77)90008-5

Wang, X., Wei, S., Wang, Y., Maung Maung, P., Hubbard, J., Banerjee, P., Huang, B.S., Moe Oo, K., Bodin, T., Foster, A., Almeida, R., 2019. A 3-D Shear Wave Velocity Model for Myanmar Region. Journal of Geophysical Research: Solid Earth 124, 504-526.

10.1029/2018JB016622

Wessel, P., Smith, W.H.F., Scharroo, R., Luis, J., Wobbe, F., 2013. Generic Mapping Tools: Improved Version Released. Eos, Transactions American Geophysical Union 94, 409-410. 10.1002/2013eo450001

Wu, Q.-J., Tian, X.-B., Zhang, N.-L., Li, W.-P., Zeng, R.-S., 2003. Receiver function estimated by maximum entropy deconvolution. Acta Seismologica Sinica 16, 404-412. 10.1007/s11589-003-0073-y

Wu, S., Yao, J., Wei, S., Hubbard, J., Wang, Y., Min Htwe, Y.M., Thant, M., Wang, X., Wang, K., Liu, T., Liu, Q., Tong, P., 2021. New insights into the structural heterogeneity and geodynamics of the Indo-Burma subduction zone from ambient noise tomography. Earth and Planetary Science Letters 562, 116856. 10.1016/j.epsl.2021.116856

Yao, H., van Der Hilst, R.D., de Hoop, M.V., 2006. Surface-wave array tomography in SE Tibet from ambient seismic noise and two-station analysis — I. Phase velocity maps. Geophysical Journal International 166, 732-744. 10.1111/j.1365-246X.2006.03028.x

Yao, J., Liu, S., Wei, S., Hubbard, J., Huang, B.-S., Chen, M., Tong, P., 2021. Slab Models Beneath Central Myanmar Revealed by a Joint Inversion of Regional and Teleseismic Traveltime Data. Journal of Geophysical Research: Solid Earth 126, e2020JB020164. 10.1029/2020JB020164

Zhang, G., He, Y., Ai, Y., Jiang, M., Mon, C.T., Hou, G., Thant, M., Sein, K., 2021. Indian continental lithosphere and related volcanism beneath Myanmar: Constraints from local earthquake tomography. Earth and Planetary Science Letters 567, 116987. 10.1016/j.epsl.2021.116987

Zhang, J.e., Xiao, W., Windley, B.F., Wakabayashi, J., Cai, F., Sein, K., Wu, H., Naing, S., 2018. Multiple alternating forearc- and backarc-ward migration of magmatism in the Indo-Myanmar Orogenic Belt since the Jurassic: Documentation of the orogenic architecture of eastern Neotethys in SE Asia. Earth-Science Reviews 185, 704-731. 10.1016/j.earscirev.2018.07.009

Zhang, L.Y., Fan, W.M., Ding, L., Ducea, M.N., Pullen, A., Li, J.X., Sun, Y.L., Yue, Y.H., Cai, F.L., Wang, C., Peng, T.P., Sein, K., 2020. Quaternary Volcanism in Myanmar: A Record of Indian Slab Tearing in a Transition Zone From Oceanic to Continental Subduction. Geochemistry, Geophysics, Geosystems 21, e2020GC009091. 10.1029/2020gc009091

Zhang, P.-Z., Shen, Z., Wang, M., Gan, W., Bürgmann, R., Molnar, P., Wang, Q., Niu, Z., Sun, J., Wu, J., Hanrong, S., Xinzhao, Y., 2004. Continuous deformation of the Tibetan Plateau from global positioning system data. Geology 32. 10.1130/g20554.1

Zhao, J., Yuan, X., Liu, H., Kumar, P., Pei, S., Kind, R., Zhang, Z., Teng, J., Ding, L., Gao, X., Xu, Q., Wang, W., 2010. The boundary between the Indian and Asian tectonic plates below Tibet. Proc Natl Acad Sci U S A 107, 11229-11233. 10.1073/pnas.1001921107

Zheng, T., He, Y., Ding, L., Jiang, M., Ai, Y., Mon, C.T., Hou, G., Sein, K., Thant, M., 2020. Direct structural evidence of Indian continental subduction beneath Myanmar. Nature Communications 11, 1944. 10.1038/s41467-020-15746-3

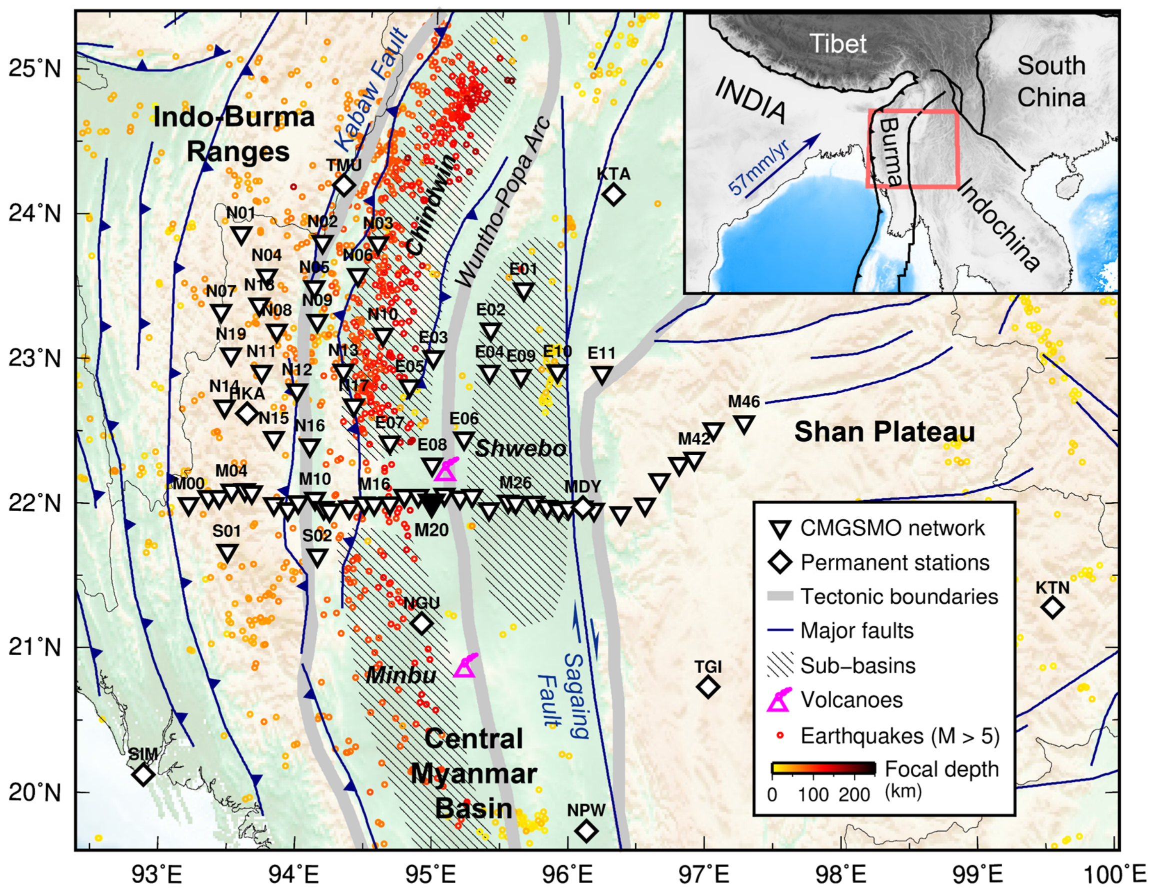

Figure 1. Overview map of the study region, showing topography, seismic stations, tectonic boundaries, major faults (Taylor and Yin, 2009), sub-basins (Licht et al., 2018), Holocene volcanoes and relocated seismicity (ISC-EHB Bulletin 1964-2016, Engdahl et al., 2020). Station M20 that is filled in black is used for plotting cross correlation records in Figure S1. Tectonics of SE Asia is shown in the inset map. The red rectangle outlines the present study region. The blue arrow denotes the plate motion of India relative to Eurasia in the HS3-NUVEL 1A model (Gripp and Gordon, 2002).

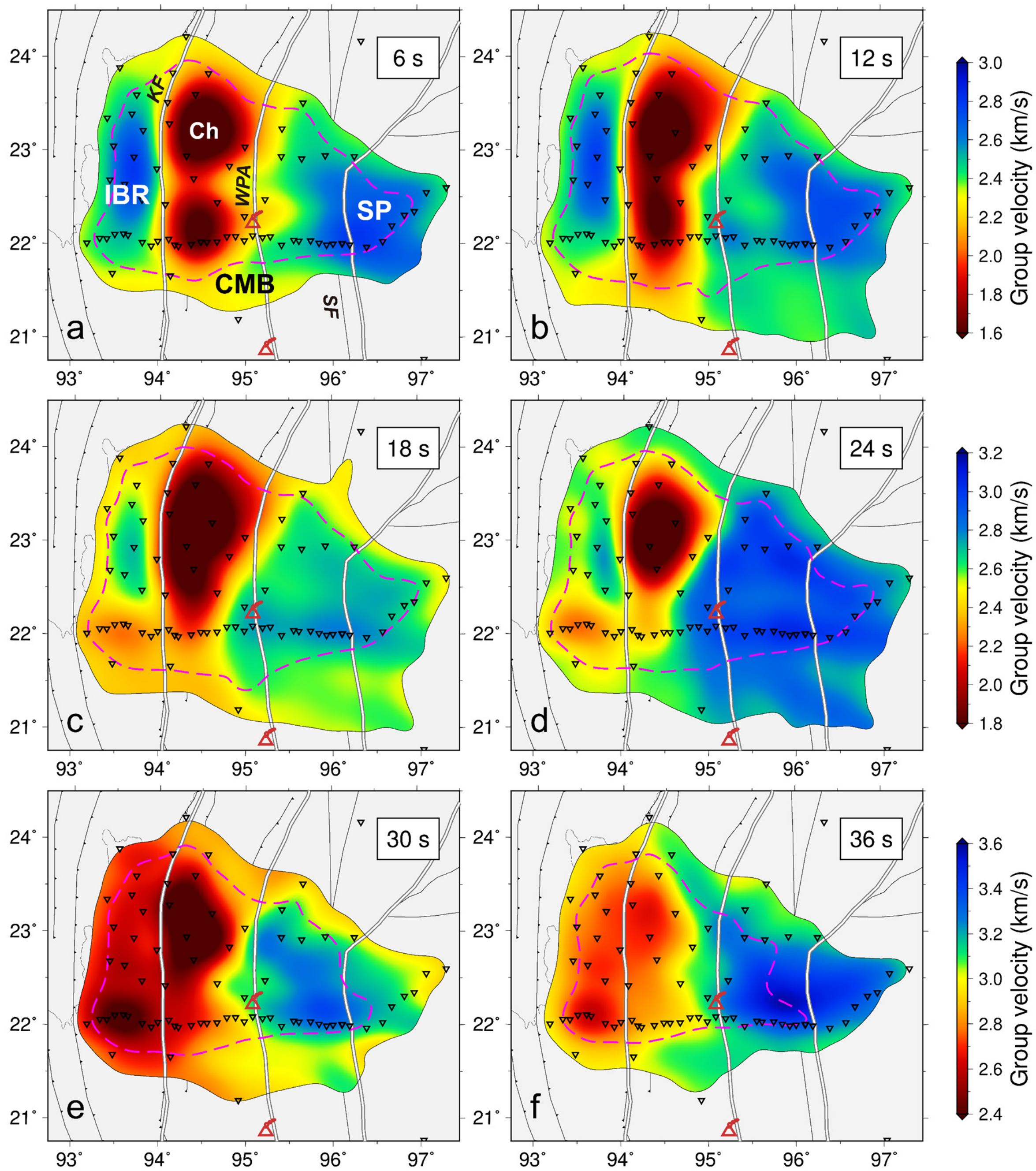

Figure 2. 2-D group velocity maps at representative periods derived from ambient noise tomography. Pink dashed lines outline regions with uncertainties less than 0.06 km/s in group velocity maps. Thick white lines mark major tectonic boundaries. Seismic stations and Holocene volcanoes are also shown. Abbreviations: IBR, the Indo-Burma Ranges; CMB, the Central Myanmar Basin; SP, the Shan Plateau; Ch, the Chindwin basin; KF, the Kabaw Fault; WPA, the Wuntho-Popa Arc; SF, the Sagaing Fault.

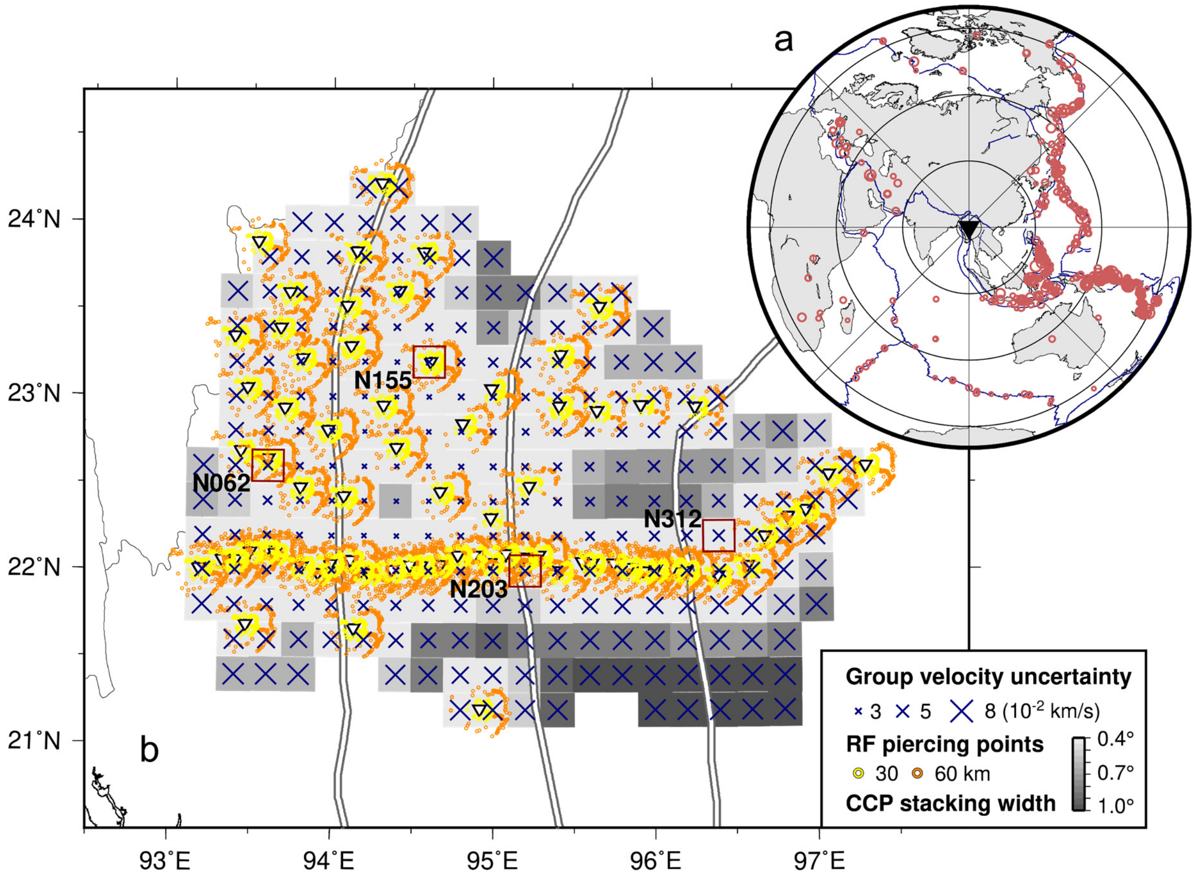

Figure 3. (a) Map of event distribution used for RF calculation. Sizes of circles indicate the earthquake magnitude. (b) Blue crosses denote grid nodes where 1-D shear velocity structure is inverted for. Sizes of crosses represent the inverted group velocity uncertainty averaged at the period band of 3-40 s. RF piercing points at 30 and 60 km depths are shown as yellow and orange circles, respectively. The underlying grayscale map shows the lateral cell width for CCP stacking at 30 km depth. The minimum width of 0.4° is applied at the majority of nodes. Final joint inversion outcomes at four representative nodes marked in red squares are plotted in Figure 5.

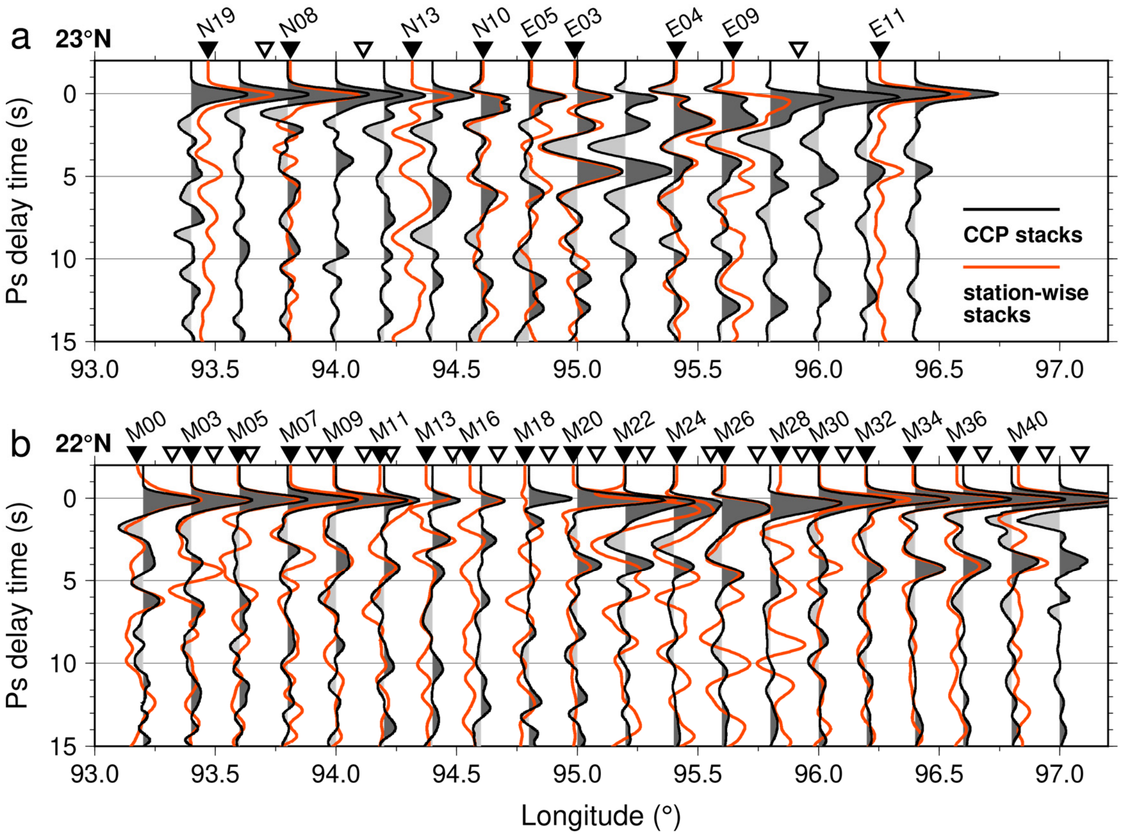

Figure 4. Stacked RF waveforms along 23°N (a) and 22°N (b). All the nearby stations are projected and shown as triangles atop each profile. Black curves with gray shades represent CCP stacks constructed at each grid nodes. As a comparison, stacked RFs at selected single stations (filled triangles with station codes) are shown as red curves. The independently derived station-wise stacks are produced in two steps. First, all the RFs from one station are linearly stacked at back-azimuth interval of 10°. Then, the bin-averaged RFs are stacked again without moveout correction (see text for further explanations).

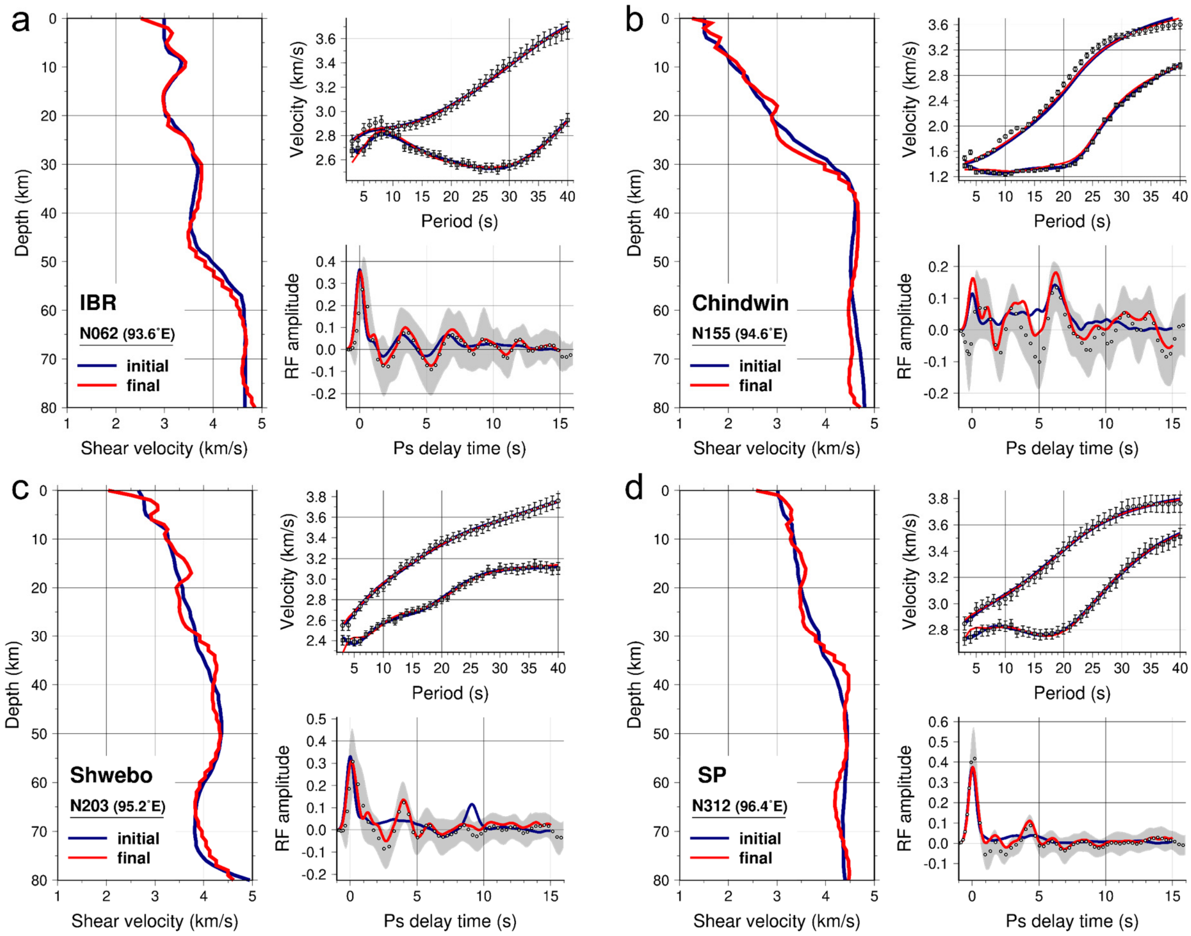

Figure 5. Examples of final joint inversion results at representative nodes of N062 (a), N155 (b), N203 (c) and N312 (d). In each sub-figure, the left panel displays the initial Bayesian probabilistic model (blue curve) and the final joint inversion model (red curve). The right-upper panel shows surface wave dispersion fits. Discrete symbols represent dispersion measurements. Error bars denote uncertainties estimated by ambient noise tomography. The blue and red curves represent synthetic dispersion curves calculated by the initial and the final inversion model, respectively. The right-bottom panel shows the RF fit. The observed CCP stack is delineated by discrete dots with the corresponding one standard deviation shown as the gray-shaded area. Blue and red curves are synthetics produced using the initial and the final model, respectively.

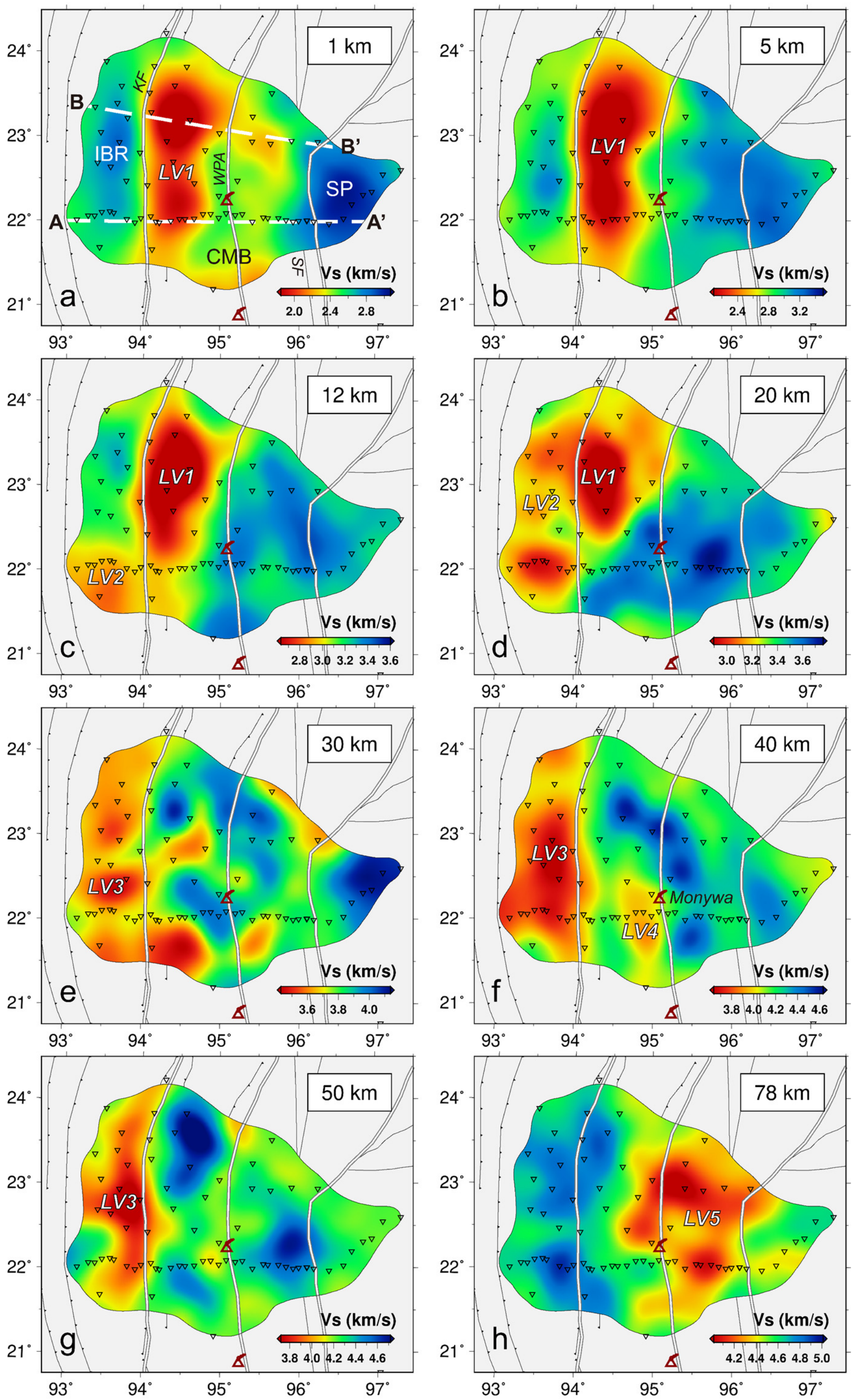

Figure 6. Shear velocity maps of central Myanmar at different depths by joint inversion of Rayleigh wave dispersion and RFs. LV1-LV5 indicate low-velocity anomalies discussed in the text. White dashed lines in a denote the locations of two vertical cross sections. Major tectonic boundaries and volcanoes are superimposed.

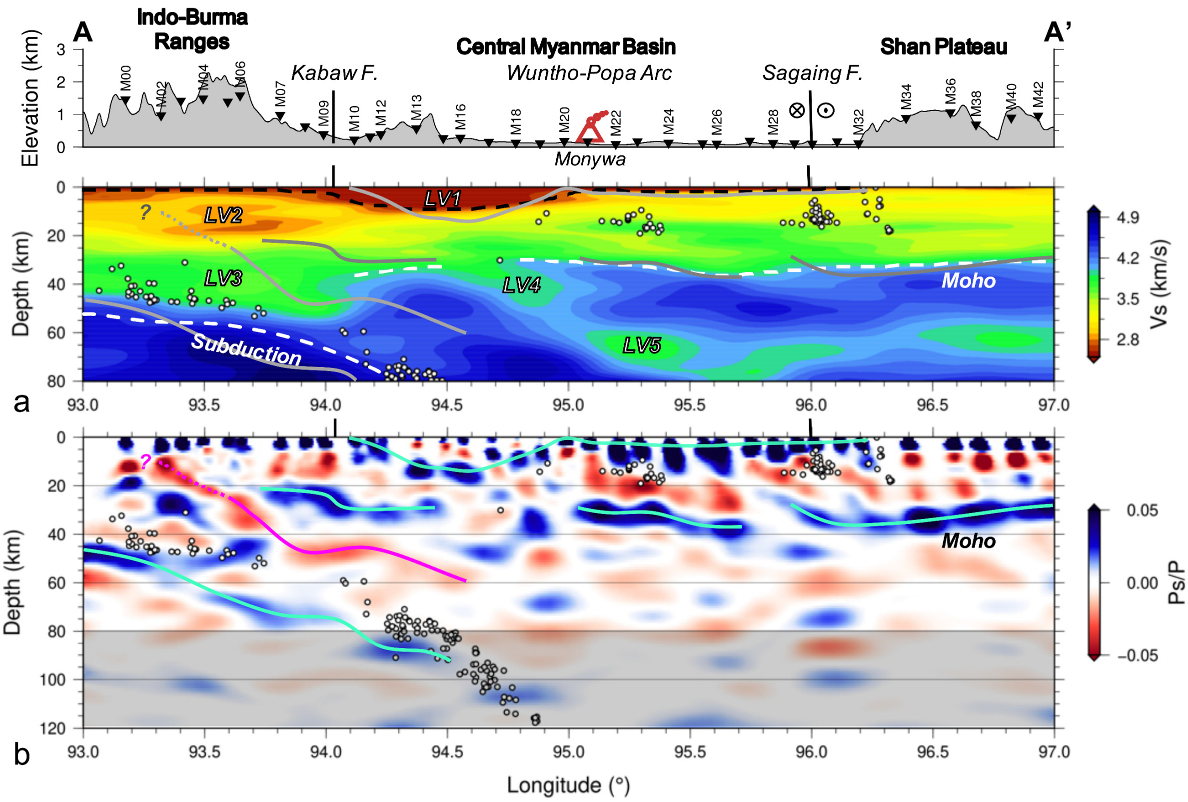

Figure 7. Vertical cross sections along profile AA' (22°N). Surface topography is plotted at the top with nearby stations and volcanoes projected onto the profile. (a) Shear velocity structure obtained from joint inversion. Dashed lines indicate the sedimentary basement (black) or the Moho (white). Gray lines are Ps conversions traced in b. LV1-LV5 indicate low-velocity anomalies discussed in the text. (b) Conventional CCP stacked profile of RFs constructed using the velocity model from a. Positive phases in blue indicate downward impedance increases, while red negative phases indicate downward impedance decreases. Pronounced positive and negative Ps conversions are highlighted by cyan and purple lines, respectively. Areas below 80 km depth are not constrained by joint inversion and are shaded in gray. White dots are relocated seismicity (Mon et al., 2020) within ±0.2° from the profile.

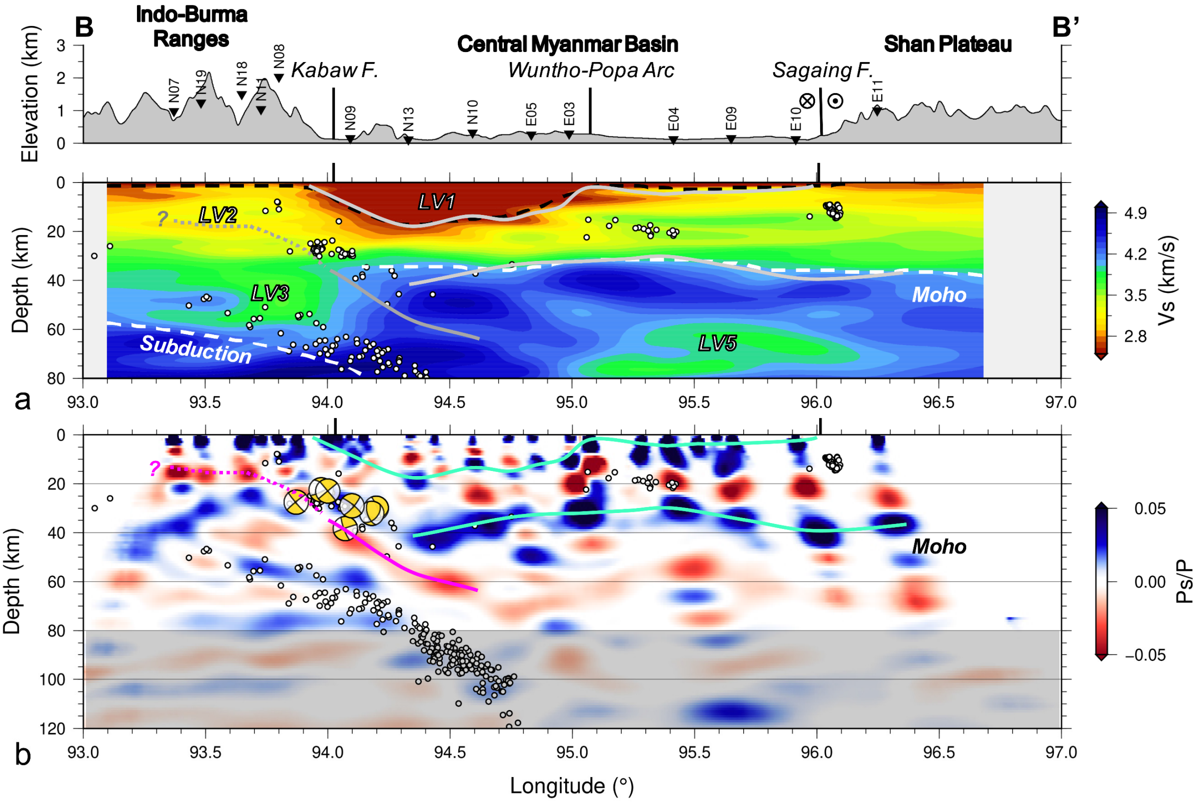

Figure 8. Same as Figure 7 but for cross sections along profile BB' (~23°N). Focal mechanisms (yellow-white beach balls) within 0.4° from the profile (Mon et al., 2020) have been projected on the vertical plane of the focal sphere in b.

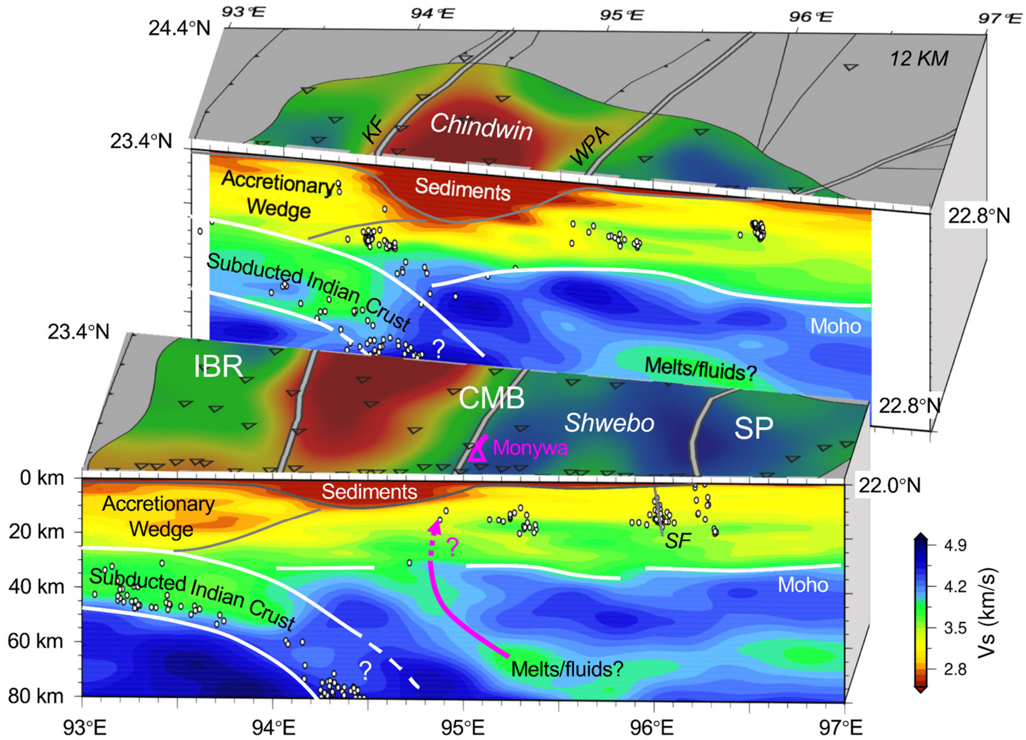

874

875 **Figure 9.** 3-D sketch summarizing the main features beneath central Myanmar from this study.
876 Two shear velocity profiles along AA' and BB' are displayed, with the horizontal shear velocity
877 section at 12 km depth showing on top. Interpretation lines are based on the results from both
878 joint inversion and CCP stacking. Abbreviations: IBR, the Indo-Burma Ranges; CMB, the
879 Central Myanmar Basin; SP, the Shan Plateau; KF, the Kabaw Fault; WPA, the Wuntho-Popa
880 Arc; SF, the Sagaing Fault. See Figures 6-8 and text for more explanations.